

Growth of Manganese Oxide Nanostructures Alters the Layout of Adhesion on a Carbonate Substrate

CHONGZHENG NA AND SCOT T. MARTIN*

School of Engineering and Applied Sciences & Department of Earth and Planetary Sciences, Harvard University, Cambridge, Massachusetts 02138

Received February 16, 2009. Revised manuscript received May 11, 2009. Accepted May 12, 2009.

Nanostructures grown under natural conditions can modify the layout of adhesion on mineral surfaces. Using force-volume microscopy and a silicon-nitride probe, we measure changes in adhesion when a patchy overgrowth of manganese oxide nanostructures forms on the surface of rhodochrosite. For the most part, the observations show that the adhesive force to the nanostructures is dominated by van-der-Waals attraction. Measurements made across an area of the surface provide a frequency distribution of adhesive forces, and the mode of this distribution is 166 pN at pH 5.0, increasing to a maximum of 692 pN at pH 7.1, followed by a decrease to 275 pN at pH 9.7. At a few sampling locations over some nanostructures, electrostatic repulsion overtakes van-der-Waals attraction and thus results in negative adhesive forces (i.e., repulsion). Local roughness causes this effect. In comparison to the oxide nanostructures, the exposed rhodochrosite substrate has negligible adhesive force with the probe over the same pH range, suggesting both weak van-der-Waals attraction and weak electrostatic repulsion over this pH range. The quantitative mapping of adhesive force applied more generally to the study of other nanostructures can lead to an improved mechanistic understanding of how nanostructure growth influences contaminant immobilization and bacterial attachment.

1. Introduction

The immobilization of metal ions, colloidal particles, and bacterial cells by lacustrine, riparian, and hypogeal minerals can be influenced by the overgrowth of nanosized surface structures (1–3). Such structures have been observed on many mineral surfaces under environmentally relevant conditions (4–9). They are often formed by heteroepitaxial nucleation and oriented growth, and their atomic arrangements and physicochemical properties may not have bulk-phase equivalents (8, 10). The morphologies of the nanostructures are guided by the underlying substrate lattices and self-limit to heights in the nanometer range. Understanding the changes in surface properties and mineral reactivity caused by nanostructure growth is important for advancing the mechanistic modeling of the fate and transport of environmental contaminants (11, 12).

Manganese oxide (MnO_x) nanostructures grown on rhodochrosite (MnCO_3) are one prototypical example of nanostructure growth that alters surface properties and mineral reactivity. Rhodochrosite is an important constituent of anoxic soils and sediments (2, 13, 14). Rhodochrosite reacts

with dissolved oxygen, causing the epitaxial overgrowth of MnO_x nanostructures (8, 10, 15). Compared to the substrate, the nanostructures have different surface potentials (16), ion mobilities (17), and interfacial forces (18). For example, although the nanostructures are only a few nanometers high (8, 10), they can have surface potentials several hundred millivolts greater than the substrate (16) and acquire 10 times more surface charge (18). As a result, the nanostructures exhibit noncontact repulsive interfacial forces of up to 100 pN and greater (compared to a baseline of 0 pN over substrate) when probed by a silicon-nitride atomic-force-microscope (AFM) tip under acidic and alkaline conditions (18).

A reasonable hypothesis, on the basis of the different noncontact interfacial forces between the oxide nanostructures and the rhodochrosite substrate, is that the contact adhesive forces also differ. The rationalization for this hypothesis is that van-der-Waals and electric forces contribute to both noncontact and contact interactions (19, 20). In comparison to the noncontact interfacial forces that affect the approach of an adsorbate to a surface, the contact adhesive force influences whether an adsorbate can readily desorb under the effect of hydraulic shear (21, 22). The adhesive force is the minimum force required for the separation of an adsorbate from a surface (21) and is, therefore, an important regulator of contaminant sorption and mobility.

Adhesive forces and their heterogeneity across a surface can be measured using force-volume microscopy (FVM). At a sampling location, the adhesive force is measured by pulling on an AFM tip that is in contact with the surface. As the tip is pulled, forces such as van-der-Waals attraction and electrostatic repulsion are balanced by the force of mechanical deflection of the tip cantilever. The adhesive force f_{adh} is, by definition, the deflective force f_{cant} on the cantilever just prior to tip–surface separation:

$$f_{\text{adh}} = f_{\text{cant}}^* \quad (1)$$

where the asterisk represents the condition of “just prior to tip–surface separation”. Measurements made of the adhesive force at each x – y lateral location provide a map $f_{\text{adh}}(x, y)$ of the heterogeneity of the adhesive forces over the oxide–carbonate surface.

The objectives of this research were to quantify the different adhesive forces over the oxide nanostructures and the exposed rhodochrosite using FVM and to separate the contribution to adhesion of electrostatic repulsion from that of van-der-Waals attraction. Specifically, we measured the adhesive forces for an ionic strength of 1 mM and varied pH from 5.0 to 9.7. Compared to our previous companion study that quantified the interfacial forces influencing adsorption (18), the present study quantifies the adhesive forces that affect desorption.

2. Experimental Methods

Manganese oxide nanostructures were grown by reacting freshly cleaved rhodochrosite samples with dissolved oxygen for 2 h at pH 6.3, as described previously (8, 16, 18). The samples were then transferred to the fluid cell of a Veeco multimode scanning probe microscope for the measurement of the adhesive force between the surface and a silicon-nitride AFM tip (Veeco DNP-S, spring constant: 48.8 pN nm^{-1}) (Supporting Information (SI) Figure S1). In the fluid cell, both the sample and the AFM tip were immersed in aqueous

* Corresponding author e-mail: scot_martin@harvard.edu.

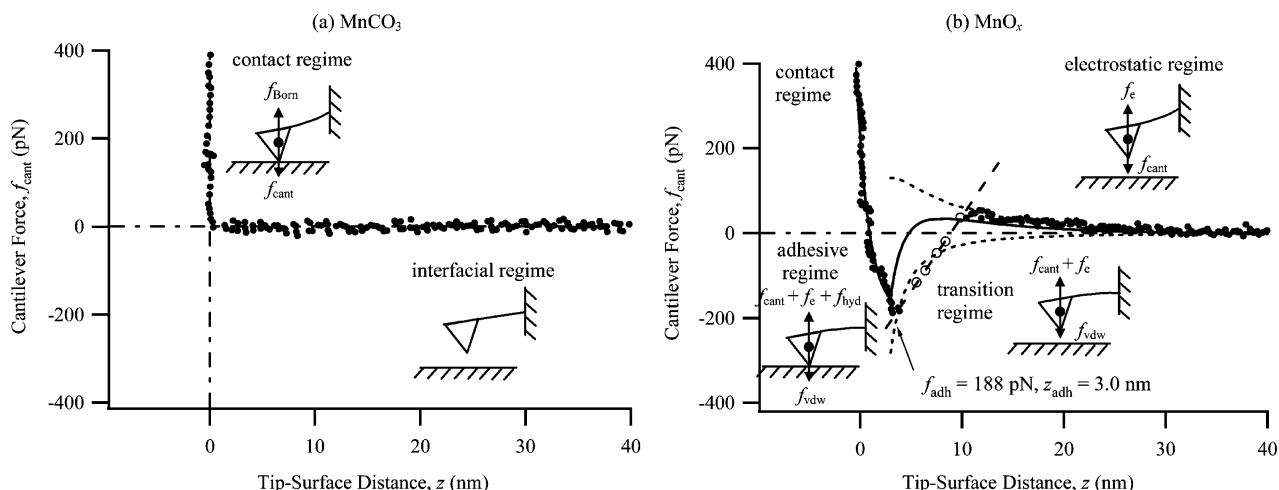


FIGURE 1. Measurements of adhesive forces. Shown are representative force–distance curves obtained as the AFM probe retracts from (a) the rhodochrosite substrate and (b) the manganese oxide nanostructures in 1 mM NaNO₃ at pH 9.7. The solid dots representing f_{cant} are measured at times when the probe is in mechanical equilibrium with the surface forces f_{vdw} , f_e , f_{Born} , and f_{hyd} . The open circles represent apparent f_{cant} values measured at times of disequilibrium. In (b), the long-dashed line is a linear fit of the open circles, and the solid and short-dashed lines are the modeled surface forces (see text). Contact, interfacial, adhesive, transition, and electrostatic regimes of z are discussed in the text. Inset cartoons show forces acting on the probe tip in each regime. The tip applies a “pulling” or “pressing” force to the surface depending on the sign of f_{cant} . Data for $f_{\text{cant}} > 400$ pN or $z > 40$ nm are omitted for clarity.

solution. The aqueous solution was adjusted to 1 mM ionic strength using sodium nitrate. The pH was adjusted between 5.0 and 9.7 using nitric acid and sodium hydroxide.

A typical experiment was performed as follows. Contact-mode microscopy was first used to locate a representative $1 \times 1 \mu\text{m}^2$ region that contained both manganese oxide nanostructures and the exposed rhodochrosite substrate (8, 10, 16–18). Force-volume microscopy, using the implementation described in ref 18, was performed to measure adhesive forces in a lateral matrix of 16×16 sampling locations. The FVM measurements were performed at $25(\pm 2)^\circ\text{C}$ after the experimental assembly had reached thermal equilibrium (23).

Each measurement of adhesive force during an FVM scan began by pressing the tip into contact with the surface using a force of ca. +1000 pN. The pressing force was applied by bringing the sample stage toward the AFM tip, which was mounted to an end of a cantilever. The fixed end of the cantilever was secured at constant height. When the tip–surface contact was established, further elevation of the sample stage pressed the tip on the surface and bent the cantilever. After the force f_{cant} reached its preset value of +1000 pN, the sample stage was gradually lowered to release the force at a rate of less than 3750 pN s^{-1} . Eventually the force reversed from pressing (i.e., a positive force) to pulling (i.e., a negative force), representing a switch of the tip–surface interaction from repulsion to attraction. While the cantilever force f_{cant} was being released, the tip–surface distance z was simultaneously obtained from cantilever deflection and the movement of the sample stage. The basic information obtained at each x – y lateral location of the FVM scan was, therefore, a set of $f_{\text{cant}}-z$ data pairs defining a force–distance curve. For each such curve, the local surface adhesion f_{adh} was determined through eq 1. Scanning in the x – y plane provided a map of $f_{\text{adh}}(x,y)$ every 15 min.

3. Results

Figure 1 shows the force on the cantilever as the rhodochrosite substrate (Figure 1a; pH 9.7) and the oxide nanostructure (Figure 1b) are retracted with the sample stage (cf. SI Figure S2). The shapes of the $f_{\text{cant}}-z$ curves in this figure reveal that the tip interacts differently with the rhodochrosite substrate compared to the oxide nanostructures. We analyze these

interactions below with the aid of force-balance analyses for the AFM tip, as illustrated by the cartoons in Figure 1.

Over rhodochrosite (Figure 1a), the force–distance curve has a sidelong “L” shape. At the beginning of surface retraction at the tip–surface distance z of 0 nm, the tip is pressed to the surface with a force f_{cant} of +1000 pN. We refer to this portion of the force–distance curve as the “contact regime”. In the contact regime, the force balance on the tip consists of f_{cant} applied by the cantilever and of the force f_{Born} of Born repulsion applied by the substrate. Born repulsion arises from the overlap of electron atmospheres (21). As surface retraction proceeds, the pressing force gradually decreases to zero while z remains unchanged within the experimental uncertainty. The vertical line of f_{cant} at z of 0 nm shows that rhodochrosite behaves as a hard surface when pressed. At the end of the contact regime (i.e., $f_{\text{cant}} = 0$ pN and $z = 0$ nm), moving the rhodochrosite surface further away from the tip results in tip–surface separation. We refer to the portion of the force–distance curve having $z > 0$ nm as the “interfacial regime”. The horizontal line of $f_{\text{cant}} = 0$ pN for $z > 0$ nm of the interfacial regime indicates that the tip experiences forces neither from the rhodochrosite surface nor from the cantilever.

For the oxide nanostructures (Figure 1b), the interfacial regime of the force–distance curve has a complex shape that can be divided into three subregimes. At the end of the contact regime, f_{cant} reverses from pressing to pulling, continues to increase for greater tip–surface distance, and reaches a maximum f_{cant}^* of 188 pN at $z \equiv z_{\text{adh}} = 3.0$ nm. This portion of the force–distance curve from 0 to z_{adh} is the “adhesive regime”, so named because the tip remains in the vicinity of the surface even as the pulling force is increased. In addition to van-der-Waals attraction and electrostatic repulsion, a hydration force f_{hyd} also contributes significantly to the tip–surface interaction in this regime (vide infra).

Further increase of the pulling force causes the tip to separate abruptly from the nanostructure. In this so-called “transition regime” (i.e., the open circles in Figure 1b), the forces of the tip–surface interactions and the force of the mechanical deflection of the cantilever do not sum to zero; therefore, unlike the other regimes, in this regime the measured cantilever force does not represent the surface force. The data pairs of f_{cant} and z can be fit by a straight line

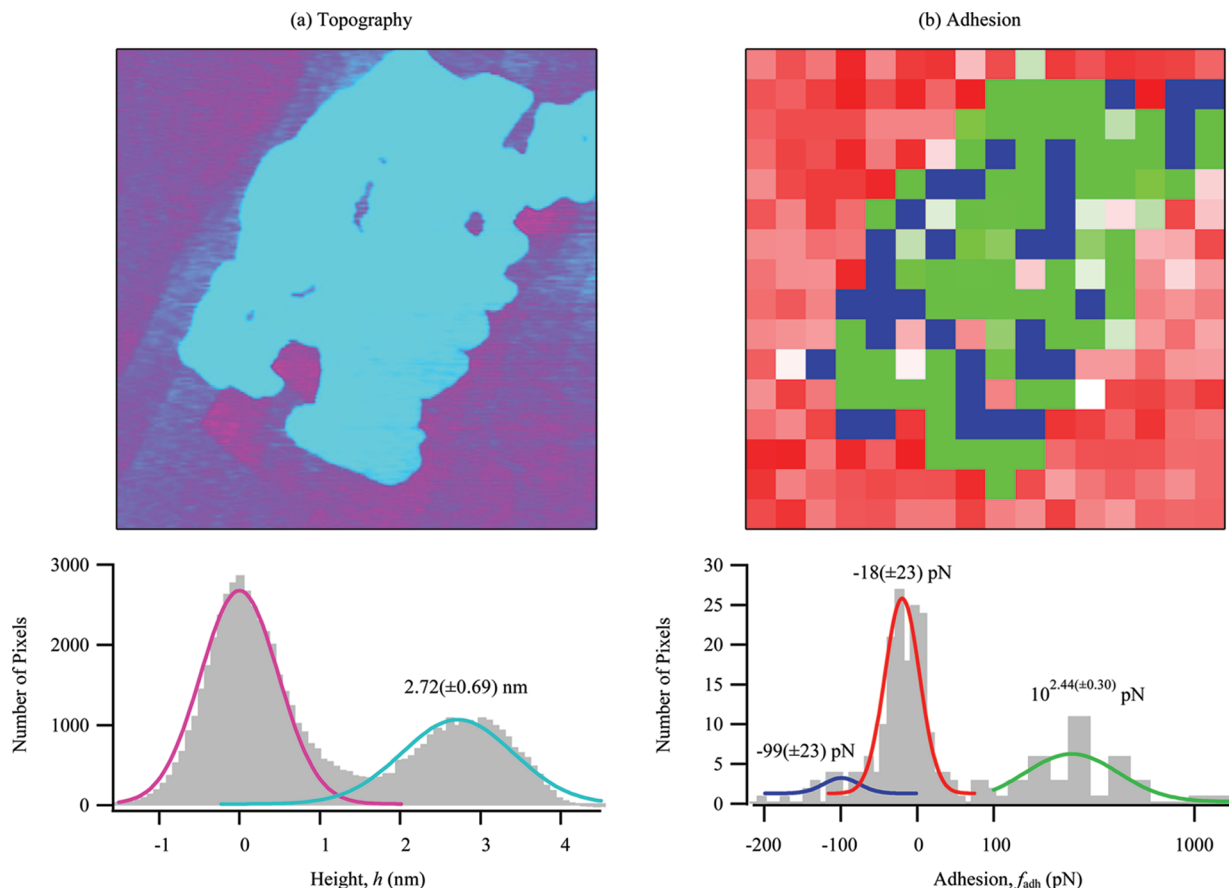


FIGURE 2. Images of (a) topography and (b) adhesion over a nanostructure-patched rhodochrosite surface in 1 mM NaNO_3 at pH 6.0. Image size: $1 \times 1 \mu\text{m}^2$. Resolution: topography, $2 \times 2 \text{ nm}^2$; adhesion, $62.5 \times 62.5 \text{ nm}^2$. Color code: Cyan, green, and blue for the oxide nanostructure and pink and red for the exposed rhodochrosite substrate. The false color of the adhesive force has a mixed scale, which is linear under 100 pN and exponential above it, as shown along the abscissa of the bottom panel of *b*. Histograms underneath the images are fit with normal distributions. $h(\text{MnO}_x)$, $h(\text{MnCO}_3)$, and $f_{\text{adh}}(\text{MnCO}_3)$ are fit by linear-normal distributions. $f_{\text{adh}}(\text{MnO}_x)$ is better represented by a log-normal distribution.

with a slope of $49.4(\pm 0.1) \text{ pN nm}^{-1}$, including an adjustment for the movement of the sample stage (cf. SI Figure S3). The magnitude of the slope agrees well with the spring constant k of the cantilever, which is indicative of the breakdown of force balance. This phenomenon is often referred to as the “snapping back” of the cantilever, which occurs when the force gradient exceeds the spring constant of the cantilever (19).

Force balance is restored for the cantilever by z of 10.4 nm, after which the force that the cantilever applies to the tip through mechanical deflection is again balanced by those related to the surface. Long-range repulsive forces (i.e., $z > 10.4 \text{ nm}$) associated with the surface are electrostatic. This portion of the force–distance curve for retraction therefore coincides with that for approach at the same location (cf. SI Figure S2). We therefore term this portion of the force–distance curve as the “electrostatic regime”. An electrostatic regime of repulsion is also consistent with our earlier work that established that both the AFM tip and the oxide nanostructures are negatively charged at pH 9.7 (18). As z further increases beyond approximately 25 nm, f_{cant} falls toward zero because the electrostatic repulsion diminishes (18).

Application of eq 1 to the observations shown in Figure 1b yields an adhesive force $f_{\text{adh}}(\text{MnO}_x)$ of 188 pN. In comparison, a typical measurement over rhodochrosite has an adhesive force of 0 pN, within experimental uncertainty. For context, literature values are 56 400, and 1760 pN for mica, gold, and silica, respectively, for adhesion to a similar tip near circumneutral pH (24). The nanostructures therefore

have appreciable adhesion, at least to the AFM tip and any chemical or biological adsorbates similar to it.

Figure 2 shows representative topography and adhesion images of a rhodochrosite surface having a manganese oxide nanostructure. In Figure 2a, the cyan color represents the nanostructure as having a height of $2.72(\pm 0.69) \text{ nm}$ above the pink color that represents the substrate ($h(\text{MnCO}_3) = 0(\pm 0.47) \text{ nm}$). Figure 2b shows the corresponding map of adhesive force f_{adh} , as obtained from the maximum pulling force for the force–distance curves collected individually at each location represented by a pixel of the image.

The map of adhesive forces in Figure 2b is color-scaled according to the histograms in the lower panel. Nanostructure material is represented in green for $f_{\text{adh}} > 0$ and in blue for $f_{\text{adh}} < 0$. The substrate is represented in red (i.e., $f_{\text{adh}} \approx 0$). Figure 2b shows that the adhesive force of the nanostructures is greater (the blue areas aside) than that of the rhodochrosite substrate. Specifically, $f_{\text{adh}}(\text{MnCO}_3) = -18(\pm 23) \text{ pN}$, $f_{\text{adh}}(\text{MnO}_x) = 219 \text{ pN}$ (range of 128–372 pN) for the green region (68% of all nanostructure pixels), and $f_{\text{adh}}(\text{MnO}_x) = -99(\pm 23) \text{ pN}$ for the blue region (32% of all nanostructure pixels). Negative adhesive forces for the blue region indicate that the tip is repulsed. This reversal from attraction to repulsion at some sampling locations over the nanostructure material is explained by the dominance of electrostatic repulsion over van-der-Waals attraction and corresponds to local nanoscale surface roughness. Local roughness changes the goodness of the

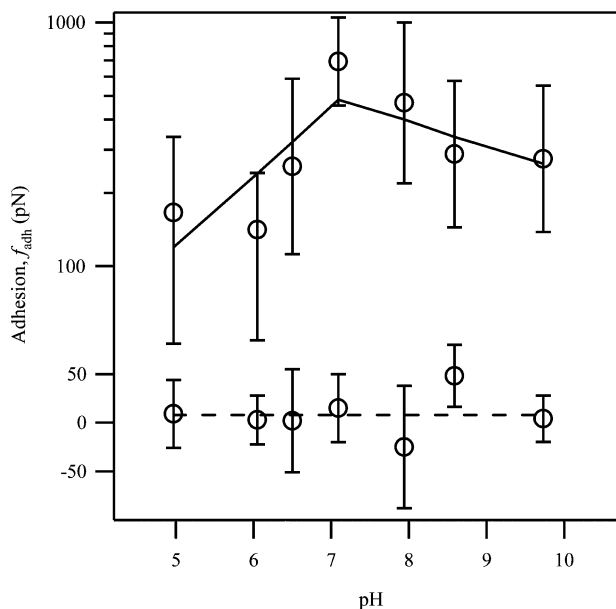


FIGURE 3. Dependence of adhesive forces on pH in 1 mM NaNO_3 . The solid lines are piecewise least-squares linear regressions of $\log f_{\text{adh}}(\text{MnO}_x)$ and pH over the green region of the nanostructures (i.e., $f_{\text{adh}} > 0$) in Figure 2b. The dashed line is the average of the surface adhesion over the exposed rhodochrosite represented in red. The regression equations (solid lines) and the average value (dashed line) are provided in the text. The ordinate of f_{adh} is a mixed linear-exponential scale having a switching point at 100 pN.

tip–surface contact and hence the ratio of the force of electrostatic repulsion to that of van-der-Waals attraction (vide infra).

Figure 3 shows the dependence of adhesive force on pH. Results, corresponding to the green and red regions in Figure 2b, are shown for the oxide nanostructures (i.e., $f_{\text{adh}} > 0$) and for the exposed rhodochrosite substrate. The central value in the frequency distribution of the adhesive forces over the nanostructures increases from 166 to 692 pN for pH from 5.0 to 7.1, reaches a maximum, and then decreases from 692 to 275 pN for pH from 7.1 to 9.7. The trend is described by a piecewise linear regression (cf. SI Table S2):

$$\log f_{\text{adh}}(\text{MnO}_x) = \begin{cases} 0.64(\pm 0.63) + 0.29(\pm 0.10)\text{pH} & \text{for pH} < 7.1 \\ 3.41(\pm 0.10) - 0.10(\pm 0.08)\text{pH} & \text{for pH} > 7.1 \end{cases} \quad (2)$$

The pH dependence cannot be attributed to nanostructure topography, which does not vary with pH (18). Using these data, we estimate at 95% confidence that $\text{pH}_{\text{pzc}}(\text{MnO}_x) = 7.1(\pm 0.4)$. The uncertainty follows from twice the uncertainty of the force measurements, as estimated using data for $z > 40$ nm (i.e., ca. 15 pN). This value of $7.1(\pm 0.4)$ agrees with $\text{pH}_{\text{pzc}}(\text{MnO}_x) = 6.5(\pm 0.7)$ estimated in earlier work that employed noncontact methods (18). In contrast to $f_{\text{adh}}(\text{MnO}_x)$, the regression of $f_{\text{adh}}(\text{MnCO}_3)$ with pH is not statistically significant (cf. SI Table S3), indicating no detectable dependence on pH. For this reason, its average is shown in Figure 3 as a horizontal dashed line representing $f_{\text{adh}}(\text{MnCO}_3) = 8(\pm 22)$ pN.

4. Discussion

Adhesion between a surface and an adsorbate is a comprehensive parameter that includes contributions by several different forces. In the following sections, our discussion is organized as follows: (1) van-der-Waals and electrostatic forces over the nanostructures (i.e., DLVO forces; Section

4.1), (2) hydration and Born forces over the nanostructures (i.e., non-DLVO forces; Section 4.2), (3) effects of surface roughness on adhesion (Section 4.3), and (4) the adhesive forces over the exposed rhodochrosite substrate (Section 4.4).

4.1. van-der-Waals and Electrostatic Forces over the Nanostructures. For the portion of the force–distance curve over which the tip and the surface are not in contact, the van-der-Waals attraction and the electrostatic repulsion can be modeled as a sphere over a plane, as described by the Derjaguin–Landau–Verwey–Overbeek (DLVO) theory (18, 19):

$$f_{\text{vdw}} = -\frac{HR}{6(z + z_0)^2} \quad (3)$$

$$f_e = \frac{4\pi R}{\epsilon\epsilon_0\kappa} \left[\sigma_{\text{tip}}\sigma_{\text{surf}}\exp(-\kappa z) + \frac{1}{2}(\sigma_{\text{tip}}^2 + \sigma_{\text{surf}}^2)\exp(-2\kappa z) \right] \quad (4)$$

The Hamaker coefficient H characterizes the dispersion interaction between the electron cloud of the nanostructure and that of the tip (25). The radius R corresponds to the curvature of the tip, with is nominally 10 nm, but can be as large as 40 nm, according to the manufacturer. The atomic spacing z_0 is 0.165 nm (21). The reciprocal κ of the Debye length characterizes the thinness of the electrical double layer next to the charged surface. The term equals 0.11 nm^{-1} for 1 mM NaNO_3 at 25 °C. Other terms in eq 4 include the dielectric constant ϵ of water, the vacuum permittivity ϵ_0 , and the charge densities σ_{tip} and σ_{surf} on the AFM tip and the surface, respectively. The term σ_{surf} is further categorized as either σ_{nano} or σ_{sub} depending on whether the tip is over the nanostructures or the remaining exposed rhodochrosite substrate, respectively. The term H is similarly subcategorized as H_{nano} or H_{sub} .

Using $\sigma_{\text{tip}} = -0.013(\pm 0.002) \text{ C m}^{-2}$ (18), we fit the data for $z > 10.4$ nm of Figure 1b by eq 4, obtaining $\sigma_{\text{nano}} = -0.005(\pm 0.0002) \text{ C m}^{-2}$ for $R = 10$ nm. The fit is shown by the positive dashed line in Figure 1b for $z > 10.4$ nm and is extrapolated to $z > 3$ nm. To consider how uncertainty in the tip radius propagates into uncertainty in σ_{nano} , we employ a log-normal probability distribution for R using a mode of 10 nm and a geometric standard deviation of 1.5 nm (cf. SI Figure S4). This distribution is consistent with the manufacturer's specifications that the nominal and maximum values of R are 10 and 40 nm, respectively. For one standard deviation, we obtain $\sigma_{\text{nano}} = \{-0.008(\pm 0.0003) \text{ C m}^{-2}, -0.003(\pm 0.0002) \text{ C m}^{-2}\}$. The estimated σ_{nano} is consistent with the value of $-0.002(\pm 0.0005) \text{ C m}^{-2}$ estimated previously using the data of a force–distance curve obtained on approach (18). In that earlier work, however, the adhesive regime was not considered. Reanalysis of those earlier data yields an updated estimate of $-0.003(\pm 0.0005) \text{ C m}^{-2}$.

Application of eqs 3 and 4 to the adhesive regime of Figure 1b, in conjunction with the relationship $f_{\text{adh}} = f_{\text{cant}}^* = f_{\text{vdw}}(z_{\text{adh}}) + f_e(z_{\text{adh}})$, allows the Hamaker coefficient to be estimated. Using $f_{\text{adh}} = 188(\pm 15)$ pN, $f_e(z_{\text{adh}}) < 180(\pm 23)$ pN, $z_{\text{adh}} = 3.0(\pm 0.42)$ nm, and R of $10(\times/\div 1.5)$ nm, we calculate that $12(\pm 6) \times 10^{-19} \text{ J} < H_{\text{nano}} < 22(\pm 11) \times 10^{-19} \text{ J}$. This range brackets an estimate of $7(\pm 1) \times 10^{-19} \text{ J}$ obtained using complementary data of a force–distance curve obtained on approach (i.e., ref 18 with reanalysis described above). For a central value H_{nano} of $17(\pm 9) \times 10^{-19} \text{ J}$, the contributions of $f_{\text{vdw}}(z)$ and $f_e(z < 10.4 \text{ nm})$ to the force–distance curve are represented in Figure 1b by the dashed lines. The magnitude of H_{nano} is characteristic of semiconducting and conducting materials. For comparison, Hamaker coefficients of insulators are around 10^{-20} J (19). An implication of semiconducting properties for the oxide nanostructures is consistent with our previous observation that these structures have greater

surface potentials than the exposed rhodochrosite, a relationship suggestive of *n*-type behavior (16).

Figure 3 shows the dependence of the adhesive force on pH. The adhesive force is expected to depend on pH because of changes in surface charge density with pH. An assumption of constant van-der-Waals attraction across the experimental pH range, in conjunction with the trends observed in Figure 3, implies that the tip and the oxide nanostructures are similarly charged from pH 5.0 to 7.1(±0.4), that they undergo a charge reversal together at pH 7.1(±0.4), and that they become similarly charged again from pH 7.1(±0.4) to 9.7. This conclusion agrees with our earlier work that established that both the AFM tip and the oxide nanostructures are positively charged under acidic conditions, uncharged under circumneutral conditions, and negatively charged under alkaline conditions (18). The implication is that the surface adhesion is at a maximum at pH of 7.1(±0.4) because the electrostatic repulsion is at a minimum between uncharged objects.

4.2. Hydration and Born Forces over the Nanostructures. The force–distance curve in the adhesive regime (i.e., $0 < z < 3.0$ nm) cannot be explained solely by the sum of the van-der-Waals and electrostatic forces, as can be inferred by comparison of the extrapolation of their sum in Figure 1b (i.e., extrapolating the solid curve for $z > 3.0$ nm to $z < 3.0$ nm) to the collected data. The explanation is that at these close distances a hydration force develops. The hydration force arises in the case of a tip–surface distance comparable to the size of a water molecule (ca. 0.3 nm (26)). For 3 nm of tip–surface separation, for example, 10 layers of water molecules fit inbetween (26). Tip retraction requires that additional water molecules must enter the void space, leading to an oscillation between a repulsive force (because of the elastic expansion of the water layers) and an attractive force (because of the negative pressure created by the void space prior to water occupancy) (27). The compression of water molecules between the tip and the surface in the presence of strong tip–surface attraction (i.e., adhesion) leads to an exponential repulsive force law. This form represents extended (X-)DLVO theory (28). Further extensions, such as how surface charge responds to the change of water layer thickness and the associated readjustment of counterions in solution, are beyond the scope of this paper. Empirically, $f_{\text{cant}} = f_{\text{vdw}} + f_e + f_{\text{hyd}}$ can be fit to the observations as follows: $f_{\text{cant}} = -187(\pm 30) + 419(\pm 33)\exp[-0.85(\pm 0.13)z]$ for $z < 3.0$ nm. The solid curve for $z < 3.0$ nm in Figure 1b represents this equation.

In the contact regime, the tip–surface interaction is dominated by Born repulsion. Born repulsion decays as $(z_0/z)^8$, where z_0 is the atomic spacing (ca. 0.165 nm) (21). Our experimental uncertainty of 0.3 nm compared to the magnitude of z_0 implies that the Born repulsion varies by a factor of 100 within our capability for measurement. Hence, we represent the Born repulsion by a vertical line near $z = 0$ nm in Figure 1b.

4.3. Effects of Surface Roughness on Adhesion to the Nanostructures. We have so far described the force laws for nearly 70% of the nanostructure surfaces that have adhesive forces greater than zero (i.e., the green areas in Figure 2b). We now consider why approximately 30% of the nanostructure surfaces have negative rather than positive adhesive forces (i.e., the blue areas in Figure 2b and cf. SI Figure S5). As shown by the histogram of Figure 2b, the bifurcation between positive and negative adhesive forces is distinct (i.e., there is little overlap of the distributions at 0 pN). The dichotomy of the force modes suggests that surface roughness plays an important role in the tip–nanostructure interactions (29). Surface roughness h_{rms} can be represented by the root-mean-square of the surface topography, and $h_{\text{rms}} = 0.69(\pm 0.10)$ nm for Figure 2b. The uncertainty in parentheses is estimated

from the uncertainties in the topography measurements. Using eqs 3 and 4, we calculate $f_{\text{vdw}} + f_e$ at $z = z_{\text{rms}}$ to estimate the expected force at locations for which full contact is inhibited by local roughness. The roughness-adjusted tip–surface separation z_{rms} is estimated from h_{rms} , as follows: $z_{\text{rms}} = z_{\text{adh}}\{[(1 + R/(1.48h_{\text{rms}}))]^{-1} + (1 + 1.48h_{\text{rms}}/z_0)^{-2}\}^{-1/2} = 5.17(\pm 0.59)$ nm (29). For this value of z_{rms} , a repulsive f_{adh} of $-44(\pm 48)$ pN is expected, which is in line with the experimental value of $-99(\pm 23)$ pN.

4.4. Adhesive Forces over Rhodochrosite. Compared to the forces over the oxide nanostructures, both van-der-Waals attraction and electrostatic repulsion are much weaker over the rhodochrosite substrate, as implied by the sidelong L-shaped force–distance curve in Figure 1a (pH 9.7). Taking the uncertainty of the force measurements as the upper limit of the van-der-Waals attraction (i.e., $f_{\text{vdw,max}}(\text{MnCO}_3) = -15$ pN), we constrain eq 3 to conclude that $H_{\text{sub}} < 8.8(\pm 0.6) \times 10^{-20}$ J. In this calculation, we use $(z + z_0) = z_{\text{rms}} = 3.1(\pm 0.1)$ nm, as obtained for a local surface roughness $h_{\text{rms}}(\text{MnCO}_3) = 0.47(\pm 0.10)$ nm for the rhodochrosite surface. As a point of comparison, the Hamaker coefficient of calcite (CaCO_3) is 2.5×10^{-20} J (30). Because the van-der-Waals attraction between rhodochrosite and the AFM tip is below the detection limit, no adhesion to rhodochrosite is observed for the entire range of investigated pH, as shown in Figure 3 by the flat dashed line.

5. Implications for Environmental Systems

The results of this study show that the growth of manganese oxide nanostructures transforms a nonadhesive substrate into a surface that is patched with regions of strong adhesive forces. Similar nanostructures in the environment can facilitate adsorbate adhesion, serving as centers that can resist the hydraulic shear that influences the release of adsorbates back to natural waters. The surface adhesion ranges from 141 to 685 pN for the investigated nanostructures in the tested pH range. Overcoming this adhesion by hydraulic shear would require flow or turbulence having velocities greater than 0.7 to 3.6 m s⁻¹ (22). These velocities are much greater than typical values of several meters per day in subsurface aquifers or of several meters per hour in filter beds used in water and wastewater treatment (31). Hence, under some circumstances the growth of nanostructures can facilitate the irreversible uptake of adsorbates.

Acknowledgments

We are grateful for support received from the Chemical Sciences, Geosciences, and Biosciences Division of the Office of Basic Energy Sciences in the U.S. Department of Energy and the Akatsuka Group, Japan.

Supporting Information Available

Table S1: Chemistry of 1-mM experimental solution. Table S2: Piecewise linear regression of $f_{\text{adh}}(\text{MnO}_x)$ and pH for the data shown in Figure 3. Table S3: *t*-Test on the regressions of $f_{\text{adh}}(\text{MnCO}_3)$ with pH. Figure S1: Experimental setup for the measurement of force–distance curves. Figure S2: Raw data corresponding to the force–distance curves shown in Figure 1. Figure S3: Linear regression of the transition data in Figure 1b. Figure S4: Uncertainty in the AFM tip radius. Figure S5: A representative force–distance curve showing that electrostatic repulsion dominates over van-der-Waals attraction. Figure S6: Three sets of representative force curves. Figure S7: One set of topography and adhesion images at pH 9.5. This material is available free of charge via the Internet at <http://pubs.acs.org>.

Literature Cited

- (1) Brown, G. E.; Foster, A. L.; Ostergren, J. D. Mineral surfaces and bioavailability of heavy metals: A molecular-scale perspective. *Proc. Natl. Acad. Sci. U. S. A.* **1999**, *96*, 3388–3395.
- (2) La Force, M. J.; Hansel, C. M.; Fendorf, S. Seasonal transformations of manganese in a palustrine emergent wetland. *Soil Sci. Soc. Am. J.* **2002**, *66*, 1377–1389.
- (3) Kim, S. B.; Park, S. J.; Lee, C. G.; Choi, N. C.; Kim, D. J. Bacteria transport through goethite-coated sand: Effects of solution pH and coated sand content. *Colloid Surf., B* **2008**, *63*, 236–242.
- (4) Lea, A. S.; Hurt, T. T.; El-Azab, A.; Amonette, J. E.; Baer, D. R. Heteroepitaxial growth of a manganese carbonate secondary nano-phase on the (10 $\bar{1}$ 4) surface of calcite in solution. *Surf. Sci.* **2003**, *524*, 63–77.
- (5) Astilleros, J. M.; Pina, C. M.; Fernandez-Diaz, L.; Prieto, M.; Putnis, A. Nanoscale phenomena during the growth of solid solutions on calcite {1014} surfaces. *Chem. Geol.* **2006**, *225*, 322–335.
- (6) Murdaugh, A. E.; Liddelow, M.; Schmidt, A. M.; Manne, S. Two-dimensional crystal growth from undersaturated solutions. *Langmuir* **2007**, *23*, 5852–5856.
- (7) Shtukenberg, A. G.; Astilleros, J. M.; Putnis, A. Nanoscale observations of the epitaxial growth of hashemite on Barite (001). *Surf. Sci.* **2005**, *590*, 212–223.
- (8) Jun, Y. S.; Kendall, T. A.; Martin, S. T.; Friend, C. M.; Vlassak, J. J. Heteroepitaxial nucleation and oriented growth of manganese oxide islands on carbonate minerals under aqueous conditions. *Environ. Sci. Technol.* **2005**, *39*, 1239–1249.
- (9) Usher, C. R.; Baltrusaitis, J.; Grassian, V. H. Spatially resolved product formation in the reaction of formic acid with calcium carbonate (10 $\bar{1}$ 4): The role of step density and adsorbed water-assisted ion mobility. *Langmuir* **2007**, *23*, 7039–7045.
- (10) Duckworth, O. W.; Martin, S. T. Role of molecular oxygen in the dissolution of siderite and rhodochrosite. *Geochim. Cosmochim. Acta* **2004**, *68*, 607–621.
- (11) Feng, X. H.; Zhai, L. M.; Tan, W. F.; Liu, F.; He, J. Z. Adsorption and redox reactions of heavy metals on synthesized Mn oxide minerals. *Environ. Pollut.* **2007**, *147*, 366–373.
- (12) Nelson, Y. M.; Lion, L. W.; Ghiorse, W. C.; Shuler, M. L. Production of biogenic Mn oxides by *Leprothrix discophora* SS-1 in a chemically defined growth medium and evaluation of their Pb adsorption characteristics. *Appl. Environ. Microbiol.* **1999**, *65*, 175–180.
- (13) Calvert, S. E.; Pedersen, T. F. Sedimentary geochemistry of manganese: Implications for the environment of formation of manganiferous black shales. *Econ. Geol. Bull. Soc. Econ. Geol.* **1996**, *91*, 36–47.
- (14) Huckriede, H.; Meischner, D. Origin and environment of manganese-rich sediments within black-shale basins. *Geochim. Cosmochim. Acta* **1996**, *60*, 1399–1413.
- (15) Jun, Y. S.; Martin, S. T. Cobalt alters the growth of a manganese oxide film. *Langmuir* **2006**, *22*, 2235–2240.
- (16) Na, C.; Kendall, T. A.; Martin, S. T. Surface-potential heterogeneity of reacted calcite and rhodochrosite. *Environ. Sci. Technol.* **2007**, *41*, 6491–6497.
- (17) Kendall, T. A.; Na, C.; Martin, S. T. Electrical properties of mineral surfaces for increasing water sorption. *Langmuir* **2008**, *24*, 2519–2524.
- (18) Na, C. Z.; Martin, S. T. Interfacial forces are modified by the growth of surface nanostructures. *Environ. Sci. Technol.* **2008**, *42*, 6883–6889.
- (19) Butt, H. J.; Cappella, B.; Kappl, M. Force measurements with the atomic force microscope: Technique, interpretation and applications. *Surf. Sci. Rep.* **2005**, *59*, 1–152.
- (20) Leite, F. L.; Herrmann, P. S. P. Application of atomic force spectroscopy (AFS) to studies of adhesion phenomena: a review. *J. Adhes. Sci. Technol.* **2005**, *19*, 365–405.
- (21) Israelachvili, J. N. *Intermolecular and Surface Forces*, 2nd ed.; Academic Press: Boston, 1991.
- (22) Hiemenz, P. C.; Rajagopalan, R. *Principles of Colloid and Surface Chemistry*. 3rd ed.; Marcel Dekker: New York, 1997.
- (23) Wenzler, L. A.; Moyes, G. L.; Beebe, T. P. Improvements to atomic force microscopy cantilevers for increased stability. *Rev. Sci. Instrum.* **1996**, *67*, 4191–4197.
- (24) Cappella, B.; Dietler, G. Force-distance curves by atomic force microscopy. *Surf. Sci. Rep.* **1999**, *34*, 1–104.
- (25) Butt, H. J. Electrostatic interaction in scanning probe microscopy when imaging in electrolyte solutions. *Nanotechnology* **1992**, *3*, 60–68.
- (26) Ewing, G. E. Ambient thin film water on insulator surfaces. *Chem. Rev.* **2006**, *106*, 1511–1526.
- (27) Israelachvili, J. N.; Pashley, R. M. Molecular layering of water at surfaces and origin of repulsive hydration forces. *Nature* **1983**, *306*, 249–250.
- (28) Brant, J. A.; Childress, A. E. Membrane-colloid interactions: Comparison of extended DLVO predictions with AFM force measurements. *Environ. Eng. Sci.* **2002**, *19*, 413–427.
- (29) Rabinovich, Y. I.; Adler, J. J.; Ata, A.; Singh, R. K.; Moudgil, B. M. Adhesion between nanoscale rough surfaces - I. Role of asperity geometry. *J. Colloid Interface Sci.* **2000**, *232*, 10–16.
- (30) Bergstrom, L. Hamaker constants of inorganic materials. *Adv. Colloid Interface Sci.* **1997**, *70*, 125–169.
- (31) Logan, B. E. *Environmental Transport Processes*; Wiley: New York, 1999.

ES900500K